Journal of Power Sources 191 (2009) 259–268

Contents lists available at ScienceDirect

Journal of Power Sources

journal homepage: www.elsevier.com/locate/jpowsour

Investigation of the effects of the anisotropy of gas-diffusion layers on heat and water transport in polymer electrolyte fuel cells

Hyunchul Ju*

School of Mechanical Engineering, Inha University, 253 Yonghyun-Dong, Nam-Gu, Incheon 402-751, Republic of Korea

ARTICLE INFO

Article history:
Received 13 November 2008
Received in revised form 14 January 2009
Accepted 28 January 2009
Available online 21 February 2009

Keywords:
Polymer electrolyte fuel cell
Gas-diffusion layer
Anisotropy
Two-phase transport
Contact resistance
Numerical model

ABSTRACT

The aim of this work is to study the effects of gas-diffusion layer (GDL) anisotropy and the spatial variation of contact resistance between GDLs and catalyst layers (CLs) on water and heat transfer in polymer electrolyte fuel cells (PEFCs). A three-dimensional, two-phase, numerical PEFC model is employed to capture the transport phenomena inside the cell. The model is applied to a two-dimensional cross-sectional PEFC geometry with regard to the in-plane and through-plane directions. A parametric study is carried out to explore the effects of key parameters, such as through-plane and in-plane GDL thermal conductivities, operating current densities, and electronic and thermal contact resistances. The simulation results clearly demonstrate that GDL anisotropy and the spatial variation of GDL/CL contact resistance have a strong impact on thermal and two-phase transport characteristics in a PEFC by significantly altering the temperature, water and membrane current density distributions, as well as overall cell performance. This study contributes to the identification of optimum water and thermal management strategies of a PEFC based on realistic anisotropic GDL and contact-resistance variation inside a cell.

1. Introduction

It is well recognized in the fuel cell community that water management is a key issue in the operation of polymer electrolyte fuel cells (PEFCs). Without adequate balance between membrane dehydration and water flooding, irreversible losses due to electrolyte or mass transport resistance become excessive and exert a negative influence on the performance and durability of PEFCs. Furthermore, complex, multi-dimensional, two-phase water transport phenomena inside PEFCs are strongly affected by thermal transport due to the close interaction between water and temperature, where a significant amount of heat is released or absorbed due to the phase change of water. In addition, the evaporation and condensation rates of water are also a strong function of temperature. Therefore, it has already been mentioned in the literature [1–3] that water management in PEFCs should be coupled with thermal management to ensure the high performance and durability of PEFCs.

As shown in the scanning electron micrograph of Fig. 1, a typical carbon-paper gas-diffusion layer (GDL) in PEFCs is comprised of carbon fibres that are preferentially oriented in the in-plane direction [4] and exhibit significant anisotropy in material properties along the through-plane and in-plane directions. Therefore, it is expected that consideration of the anisotropy GDLs in a fuel-cell model is necessary for predicting more realistic and accurate temperature and water profiles in PEFCs. To date, a number of fuel-cell models of varying levels of complexity have been published [1–3,5–20]. These range from simplified, one-dimensional, fuel-cell component models to comprehensive, computational fuel-cell dynamics (CFCD) models that deal with multi-physics and multi-dimensional, multi-phase phenomena in fuel-cells. By contrast, only a few researchers [18–20] have attempted to investigate the effects of GDL anisotropy on water and heat transport phenomena. Meng [18] introduced a simplified numerical technique to approximate anisotropic electron transfer phenomena in GDLs. Once the in-plane electronic conductivity was used for both in-plane and through-plane directions in the catalyst layer (CL) and GDL, extra contact resistance was applied to the interface between a GDL together with a bipolar plate (BP) to compensate for the effect of reduced through-plane electronic resistance. Using the simplified approach, the study reported a significant improvement in numerical convergence and stability during large-scale, three-dimensional simulations. Pasaogullary et al. [19] considered anisotropic heat and species transport in their half-cell model. According to their simulation results, the effect of GDL anisotropy is indeed significant in terms of the considerable change in the water and temperature distributions in PEFCs. Bapat and Thynell [20] presented a two-dimensional, single-phase, fuel-cell model and investigated the effects of the anisotropic thermal conductivity of a GDL and membrane, and the thermal contact resistance at the interface between the GDL and the bipolar plate. They reported the considerable effects of the anisotropic thermal conductivity of a GDL on the temperature distributions in PEFCs and concluded that a high, in-plane thermal conductivity is

* Tel.: +82 32 860 7312; fax: +82 32 868 1716.
E-mail address: hcju@inha.ac.kr.

0378-7753/$ – see front matter © 2009 Elsevier B.V. All rights reserved.
doi:10.1016/j.jpowsour.2009.01.103

Nomenclature

a	water activity or effective catalyst area per unit of total volume ($m^2\ m^{-3}$)
A	area (m^2)
C_P	specific heat ($kJ\ kg^{-1}\ K^{-1}$)
C	molar concentration ($mol\ m^{-3}$)
D_k	mass diffusivity of species k ($m^2\ s^{-1}$)
EW	equivalent weight of dry membrane ($kg\ mol^{-1}$)
F	Faraday constant (96,487 $C\ mol^{-1}$)
i_0	exchange current density ($A\ m^{-2}$)
j	transfer current density ($A\ m^{-3}$)
j^i	diffusive mass flux of i phase ($kg\ m^{-2}\ s^{-1}$)
J	Leverett function
h	enthalpy per unit mass ($kJ\ kg^{-1}$)
k	thermal conductivity ($W\ m\ K^{-1}$)
k_r	relative permeability
K	hydraulic permeability (m^2)
M	molecular weight ($kg\ mol^{-1}$)
m	mass fraction
n	number of electrons in electrochemical reaction or diffusivity correction factor
n_c	catalyst coverage coefficient
n_d	electroosmotic drag coefficient
P	pressure (Pa)
P_c	capillary pressure (Pa)
RH	relative humidification of the inlet
R_u	universal gas constant ($8.314\ J\ mol^{-1}\ K^{-1}$)
s	stoichiometry coefficient in electrochemical reaction or liquid saturation
S	source term in transport equation
t	time (s)
T	temperature (K)
$\mathbf{u}$	fluid velocity and superficial velocity in porous medium ($m\ s^{-1}$)
U_o	thermodynamic equilibrium potential (V)
V	volume (m^3)
V_{cell}	cell potential (V)

Greek letters

α	transfer coefficient
δ_i	thickness of component i
ε	volume fraction of gaseous phase in porous region
ε_e	volume fraction of ionomer phase in CL
γ	advection correction factor
λ	membrane water content ($mol\ H_2O/mol\ SO_3^-$)
λ^α	relative mobility of phase α
ϕ	phase potential (V)
η	overpotential (V)
θ	contact angle (°)
μ	viscosity ($kg\ m^{-1}\ s^{-1}$)
ρ	density ($kg\ m^{-3}$)
ρ^{mem}	dry membrane density ($kg\ m^{-3}$)
υ	kinematic viscosity ($m^2\ s^{-1}$)
σ	surface tension ($N\ m^{-1}$) or electronic conductivity ($S\ m^{-1}$)
τ	viscous shear stress ($N\ m^{-2}$)
κ	ionic conductivity ($S\ m^{-1}$)
ξ	stoichiometry flow ratio

Superscripts

e	electrolyte
eff	effective value in porous region
mem	membrane
g	gas
l	liquid
ref	reference value
s	solid
sat	saturation value

Subscripts

a	anode
avg	average value
BP	bipolar plate
c	cathode
CL	catalyst layer
e	electrolyte
g	gas phase
GC	gas channel
GDL	gas-diffusion layer
H_2	hydrogen
i	species index
in	channel inlet
m	mass equation
mem	membrane
N_2	nitrogen
O_2	oxygen
ref	reference value
t	total
s	solid
sat	saturation value
w	water
Φ	potential equation
0	standard condition (298.15 K and 101.3 kPa (1 atm))

desirable as it leads to more uniform temperature distribution inside PEFCs.

Although these previous studies [18–20] demonstrated the significant influences of GDL anisotropy, some profound effects in an anisotropic GDL have not been studied in detail. These include the inter-relationship between thermal gradients and two-phase water transport, and the two-phase heat transfer that is driven by the heat release/absorption that arises from the phase change. In the present work, anisotropic, two-phase heat and water transport phenomena in PEFCs are investigated by implementing the anisotropic functions into a three-dimensional two-phase PEFC model that has been developed earlier [16,17]. In addition to studying anisotropic heat and water transport, an investigation is made of the effects of thermal contact resistance at both the GDL/CL and the GDL/BP. Previously, the effect of thermal contact resistance was studied by Bapat and Thynell [20], who applied a constant value to the contact

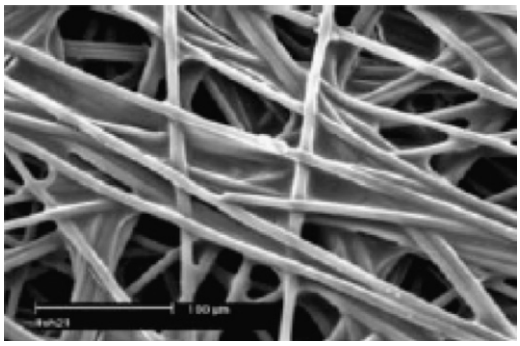

Fig. 1. SEM image of TGP-H carbon-paper GDL [4].

resistance at the interface between a GDL and BP but neglected the contact resistance at the interface between a GDL and CL. In reality, the contact resistance between a GDL and CL is expected to be more significant and vary along the in-plane direction between the gas channel (GC) and land regions. This is because the assembly clamping pressure, i.e., the compression pressure that results from torque on the bolts that clamp the fuel cell, cannot be fully applied to GDL areas under the gas channels. Therefore, in this study, the effect of the variation of the contact resistance at the interface between a GDL and CL along the in-plane direction is considered for predicting more realistic water and temperature profiles inside a PEFC. This study assists in finding appropriate water and thermal management strategies of a PEFC under realistic anisotropic GDL and contact-resistance variation.

2. Numerical model

2.1. Multi-dimensional fuel-cell model

The two-phase, non-isothermal PEFC model used for this study is based on the multi-phase mixture (M^2) model developed by Wang and Cheng [21]. The fuel-cell model has been described in detail in previous publications [16,17]; thus, only a brief summary of the conservation equations is repeated here, as follows.

2.2. Model assumptions

Employing the M^2 formulation to describe two-phase transport in PEFCs, the present two-phase PEFC model makes the following assumptions: (1) ideal gas mixtures in a single-phase region; (2) laminar flow due to small flow velocities; and (3) two-phase mist flow (i.e., homogeneous flow) in gas channels, assuming that channel flooding is minimal where tiny droplets exist and travel with the gas flow inside the gas channels.

2.3. Conservation equations

Under the above assumptions, the two-phase PEFC model is governed by the conservation of mass, momentum, chemical species, charge, and thermal energy.

Mass conservation

$$\nabla \cdot (\rho \vec{u}) = S_m \tag{1}$$

Momentum conservation

flow channels (Navier–Stokes Eqs.)

$$\frac{1}{\varepsilon^2}\nabla \cdot (\rho \vec{u}\vec{u}) = -\nabla p + \nabla \cdot \tau \tag{2}$$

porous media (Darcy's Eq.)

$$\rho \vec{u} = -\frac{K}{\nu}\nabla p \tag{3}$$

Species conservation

flow channels and porous media

$$\nabla \cdot (\gamma_i \rho m_i \vec{u}) = \nabla \cdot [\rho^g D_i^{g,eff} \nabla (m_i^g)] + \nabla \cdot [(m_i^g - m_i^l)\vec{j}^l] + S_i \tag{4}$$

water transport in membrane

$$\nabla \cdot \left(\frac{\rho^{mem}}{EW} D_w^{mem} \nabla \lambda\right) M_w - \nabla \cdot \left(n_d \frac{I}{F}\right) M_w + \nabla \cdot \left(\frac{K^{mem}}{\nu^l} \nabla P^l\right) = 0 \tag{5}$$

Charge conservation

$$\text{proton transport}: \ \nabla \cdot (\kappa^{eff} \nabla \Phi_e) + S_\Phi = 0 \tag{6}$$

$$\text{electron transport}: \ \nabla \cdot (\sigma^{eff} \nabla \Phi_s) - S_\Phi = 0 \tag{7}$$

Energy conservation

$$\nabla \cdot (\rho \vec{u} C_p^g T) = \nabla \cdot (k^{eff} \nabla T) + \nabla \cdot (h_{fg}^o \rho^l \vec{u}^l) + S_T \tag{8}$$

In the conservation equations, Eqs. ((1)–(8)), the two-phase mixture properties are defined as a function of s and $(1-s)$, which denote the volume fraction of the open pore spaces that are occupied by the liquid and gaseous phases, respectively [21].

Density [21]

$$\rho = \rho^l \cdot s + \rho^g \cdot (1-s) \tag{9}$$

In Eq. (9), the gas mixture density, ρ^g, which is described by the ideal gas law, varies with the composition (denoted here by the mass fractions, $\{m_i^g\}$). That is,

$$\rho^g = \left(\frac{P}{R_u T}\right) \frac{1}{\sum_i m_i^g / M_i} \tag{10}$$

Velocity [21]

$$\rho \vec{u} = \rho^l \vec{u}^l + \rho^g \vec{u}^g \tag{11}$$

Relative permeability

$$k_r^l = s^4 \tag{12a}$$

$$k_r^g = (1-s)^4 \tag{12b}$$

Kinematic viscosity [21]

$$\upsilon = \left(\frac{k_r^l}{\nu^l} + \frac{k_r^g}{\nu^g}\right)^{-1} \tag{13}$$

In Eq. (13), ν^g is the kinematic viscosity of a gas mixture that varies with the gas composition [22]

$$\upsilon^g = \frac{\mu^g}{\rho^g} = \frac{1}{\rho^g} \sum_{i=1}^{n} \frac{x_i \mu_i}{\sum_{j=1}^{n} x_j \Phi_{ij}}, \ where$$

$$\Phi_{ij} = \frac{1}{\sqrt{8}} \left(1 + \frac{M_i}{M_j}\right)^{-1/2} \left[1 + \left(\frac{\mu_i}{\mu_j}\right)^{1/2} \left(\frac{M_j}{M_i}\right)^{1/4}\right] \tag{14}$$

and

$$\mu_i[\mathrm{N\,s\,m^{-2}}] = \begin{cases} \mu_{H_2} = 0.21 \times 10^{-6} T^{0.66} \\ \mu_w = 0.00584 \times 10^{-6} T^{1.29} \\ \mu_{N_2} = 0.237 \times 10^{-6} T^{0.76} \\ \mu_{O_2} = 0.246 \times 10^{-6} T^{0.78} \end{cases}$$

T in Kelvin

Relative mobility [21]

$$\lambda^l = \frac{k_r^l}{\nu^l} \nu \tag{15a}$$

$$\lambda^g = 1 - \lambda^l \tag{15b}$$

The species diffusivity in the gas mixture, D_i^g, in the first term on the right-hand side of Eq. (4) is defined as follows, in order that the summation of interspecies diffusion within the gaseous phase

is equal to zero [22].

$$D_i^g = \frac{1-x_i}{\sum_{\substack{j\\ j\neq i}}^{j=n} x_j/D_{i,j}}, \text{where}$$
$$D_{i,j} = \frac{1.013\cdot 10^{-7}\cdot T^{1.75}}{p\cdot\left(\chi_i^{1/3}+\chi_j^{1/3}\right)^2}\cdot\left(\frac{1}{M_i}+\frac{1}{M_j}\right)^{1/2} \quad (16)$$
$$\chi_{H_w}=7.07,\ \chi_w=12.7,\ \chi_{N_w}=17.9,\ \chi_{O_w}=16.6$$

Note that the gaseous diffusive transport for a porous medium can be controlled by the Knudsen diffusion effect due to molecular-to-wall collision as well as molecular diffusion that is caused by molecular-to-molecular collision, as described in Eq. (16). The Knudsen diffusion coefficient can be computed according to the kinetic theory of gases as follows.

$$D_i^K = \frac{2}{3}\left(\frac{8R_uT}{\pi M_i}\right)^{1/2} r_p \quad (17)$$

The effective diffusivity of species i in the gas mixture is then obtained by combining both molecular and Knudsen diffusion effects with the effects of porosity and tortuosity of the porous medium by using the Bruggeman correlation [23].

$$D_i^{g,eff} = [\varepsilon(1-s)]^n\left(\frac{1}{D_i^g}+\frac{1}{D_i^K}\right)^{-1} \quad (18)$$

In Eq. (18), it is seen that the effective gas diffusivity, $D_i^{g,eff}$, in the two-phase region is a function of both the porosity, ε, and the liquid saturation, s.

On the other hand, the diffusive mass flux of the liquid phase, $\vec{j}^l$, which is shown in the second term on the right-hand side of Eq. (4), is expressed as a function of the capillary pressure, P_c, such that [21]:

$$\vec{j}^l = \rho^l\vec{u}^l - \lambda^l\rho\vec{u} = \frac{K}{\nu}\lambda^l\lambda^g\nabla P_c \quad (19)$$

In Eq. (19), the correlation of the capillary pressure, P_c, and the Leverett function, $J(s)$, is given by:

$$P_c = P^g - P^l = \sigma\cos\theta\left(\frac{\varepsilon}{K}\right)^{1/2} J(s) \quad (20)$$

$$J(s) = \begin{cases} 1.417(1-s)-2.120(1-s)^2+1.263(1-s)^3 & \text{if } \theta_c < 90^\circ \\ 1.417s-2.120s^2+1.263s^3 & \text{if } \theta_c > 90^\circ \end{cases} \quad (21)$$

The second term on the left-hand side of the species equation represents the advective term, in which the advection correction factor, γ_i, is given by Wang and Cheng [21], i.e.,

$$\gamma_i = \frac{\rho(\lambda^l m_i^l + \lambda^g m_i^g)}{(s\rho^l m_i^l + (1-s)\rho^g m_i^g)} \quad (22)$$

The transport properties of electrolytes are correlated with the water content of the membrane, λ, which, in turn, is a function of the water activity, a, as follows [24].

$$a = \frac{C_w^g R_u T}{P_{sat}} \quad (23)$$

$$\lambda = \begin{cases} \lambda^g = 0.043 + 17.81a - 39.85a^2 + 36.0a^3 & \text{for } 0 < a \le 1 \\ \lambda^l = 22 \end{cases} \quad (24)$$

The electro-osmotic drag coefficient, n_d, the proton conductivity in the membrane, κ, and the water diffusion coefficient in the membrane, D_w^{mem}, have been reported by Springer et al. [24].

$$n_d = \frac{2.5\lambda}{22} \quad (25)$$

$$\kappa = (0.5139\lambda - 0.326)\exp\left[1268\left(\frac{1}{303}-\frac{1}{T}\right)\right] \quad (26)$$

$$D_w^{mem} = \begin{cases} 2.692661843\cdot 10^{-10} & \text{for } \lambda \le 2 \\ \{0.87(3-\lambda)+2.95(\lambda-2)\}\cdot 10^{-10}\cdot e^{(7.9728-(2416/T))} & \text{for } 2 < \lambda \le 3 \\ \{2.95(4-\lambda)+1.642454(\lambda-3)\}\cdot 10^{-10}\cdot e^{(7.9728-(2416/T))} & \text{for } 3 < \lambda \le 4 \\ (2.563-0.33\lambda+0.0264\lambda^2-0.000671\lambda^3)\cdot 10^{-10}\cdot e^{(7.9728-(2416/T))} & \text{for } 4 < \lambda \le \lambda_{a=1}^g \end{cases} \quad (27)$$

2.4. Source terms and physicochemical relations

In the conservation equations, Eqs. ((1)–(8)), S_m, S_i, S_Φ and S_T that are summarized in Table 1 denote their corresponding source/sink terms for mass, species, charge and heat, respectively. These source terms result from the electrochemical reactions, the hydrogen oxidation reaction (HOR) in the anode CL, and the oxygen reduction reaction (ORR) in the cathode CL, respectively, which are represented by kinetic expressions as follows.

$$\text{HOR in the anode CL}: \quad j = (1-s)^{n_c} a i_{0,a}^{ref}\left(\frac{C_{H_2}}{C_{H_2,ref}}\right)^{1/2}\left(\frac{\alpha_a+\alpha_c}{R_uT}F\eta\right) \quad (36)$$

$$\text{ORR in the cathode CL}: \quad j = -(1-s)^{n_c} a i_{o,c}^{ref}\left(\frac{C_{O_2}}{C_{O_2,ref}}\right)^{3/4} \times \exp\left(-\frac{\alpha_c}{R_uT}F\eta\right) \quad (37)$$

In Eqs. (36)–(37), $(1-s)^{n_c}$ approximates the effect of decreasing electrochemically active catalyst sites due to the presence of water in the CLs.

The surface overpotential in Eqs. (36)–(37) is defined by

$$\text{HOR in the anode CL}: \quad \eta = \phi_s - \phi_e \quad (38)$$

$$\text{ORR in the cathode CL}: \quad \eta = \phi_s - \phi_e - U_o \quad (39)$$

In Eqs. (38)–(39), the thermodynamic equilibrium potential between the cathode and anode is given by [25]

$$U_o = 1.23 - 0.9\times 10^{-3}(T - 298.15) \quad (40)$$

Based on the experimental data of Parthasarathy et al. [26], the temperature dependence of the ORR kinetic parameter is approximated as follows:

$$a i_{0,c}^{ref}(T) = a i_{0,c}^{ref}(353\ \text{K})\cdot\exp\left[-\frac{E_a}{R_u}\left(\frac{1}{T}-\frac{1}{353.15}\right)\right] \quad (41)$$

Table 1
Two-phase steady-state PEFC model: source/sink terms.

Source/sink terms		
Mass	In the CLs: $S_m = \sum_i S_i + M_w \nabla \cdot (D_w^{mem}(\rho^{mem}/EW)\nabla\lambda)$	(28)
Species	For water in CLs: $S_i = M_i[-\nabla \cdot ((n_d/F)I) - (s_i j/nF)]$	(29a)
	For other species in CLs: $S_i = -M_i(s_i j/nF)$	(29b)
Charge	In the CLs: $S_\Phi = j$	(30)
Energy	In the CLs: $S_T = j(\eta + T(dU_o/dT)) + (i_e^2/\kappa^{eff})$	(31)
	In the membrane: $S_T = \frac{i_e^2}{\kappa^{eff}}$	(32)
Electrochemical reactions	$\sum_k s_i M_i^z = ne^-$, where $\begin{cases} M_i \equiv \text{chemical formula of species } i \\ s_i \equiv \text{stoichiometry coefficient} \\ n \equiv \text{number of electrons transferred} \end{cases}$	(33)
	Hydrogen oxidation reaction (HOR) in anode side: $H_2 - 2H^+ = 2e^-$	(34)
	Oxygen reduction reaction (ORR) in cathode side: $2H_2O - O_2 - 4H^+ = 4e^-$	(35)

2.5. Boundary conditions and numerical implementation

The inlet velocities in the anode and cathode gas channels can be expressed as a function of the anode and cathode stoichiometric ratios (ξ_a and ξ_c, respectively), the PEFC operating current density (I), the cross-sectional areas of the anode and cathode gas channels (A_a and A_c, respectively), and the densities of hydrogen or air gas which are respectively a function of the anode/cathode inlet pressure, temperature and humidity.

$$u_{in,a} = \frac{\xi_a(I/2F)A_{mem}M_{H_2}}{\rho_{H_2}A_a} \quad \text{and} \quad u_{in,c} = \frac{\xi_c(I/4F)A_{mem}M_{O_2}}{\rho_{O_2}A_c} \tag{42}$$

In addition, the isothermal boundary condition (80 °C for this study) is applied to the outer surfaces of the bipolar plate for temperature calculations.

The two-phase PEFC model described above is numerically implemented with a commercially available computational fluid dynamics (CFD) package, i.e., STAR-CD, based on its user-subroutine files [27].

3. Results and discussion

3.1. Simulation cases

In this study, the comprehensive two-phase, non-isothermal PEFC model is applied to two-dimensional cross-section geometry as displayed with its mesh configuration in Fig. 2, where fully humidified (100%) hydrogen and air gases are assumed along the anode and cathode GCs. The properties of the individual cell components and operating conditions are listed in Tables 2 and 3, respectively, and the relevant physical properties are summarized in Table 4. Using the cell configuration, properties and operating conditions, a parametric study has been conducted to investigate the effects of GDL anisotropy and contact resistance on the liquid saturation and temperature distribution, as well as the overall cell performance. Based on typical thermal-conductivity values of anisotropic GDLs [4,19,20], the thermal conductivity of GDLs is assumed to be 10.0 W m^{-1} K^{-1} along the in-plane direction and the through-plane thermal-conductivity value is taken to be an order of magnitude smaller than the in-plane value (thus, 1.0 W m^{-1} K^{-1} along the through-plane direction).

In terms of the GDL thermal conductivities, three types of GDL are defined for this study. The first GDL is tailored to have a through-plane thermal conductivity of 1.0 W m^{-1} K^{-1} in all directions (denoted the 'thru-plane GDL' in the following discussion). For the second GDL, the in-plane value of 10.0 W m^{-1} K^{-1} is assumed for all directions (denoted the 'in-plane GDL'). The third GDL is anisotropic and has different thermal conductivity values, viz., 1.0 W m^{-1} K^{-1} for the through-plane direction and 10.0 W m^{-1} K^{-1} for the in-plane direction (denoted the 'anisotropic GDL').

The effects of the contact resistance on heat and electron transport inside PEFCs has also been investigate. As shown in Table 2, constant values of electronic and thermal contact resistance are applied to the GDL/BP interfaces. On the other hand, as mentioned earlier, the spatial variation of the thermal and electronic contact

Table 2
Cell properties.

Description	Value
Porosity of GDLs (ε_{GDL})	0.6
Porosity of CLs (ε_{CL})	0.6
Volume fraction of ionomer in CLs (ε_{mc})	0.18
Permeability of GDLs (K_{GDL})	3.0×10^{-12} m^2
Hydraulic permeability of membrane (K_{mem})	5.0×10^{-20} m^2
Contact angle of GDLs and CLs (θ)	110°
Effective electronic conductivity in CL (σ_{CL})	1000 S m^{-1}
Effective electronic conductivity in GDL (σ_{GDL})	10,000 S m^{-1}
Effective electronic conductivity in BP (σ_{BP})	20,000 S m^{-1}
Electric contact resistance between BP and GDL ($R_{e,BP}$)	5.3 mΩ cm^2
Thermal conductivity of BP (k_{BP})	20.0 W m^{-1} K^{-1}
Thermal conductivity of membrane (k_{mem})	0.95 W m^{-1} K^{-1}
Thermal contact resistance between BP and GDL ($R_{t,BP}$)	0.75×10^{-4} cm^2 K W^{-1}

Table 3
Operating conditions.

Description	Value
Anode inlet pressure (P_a)	1.5 atm
Anode stoichiometry (ξ_a)	3
Cathode inlet pressure (P_c)	1.5 atm
Cathode stoichiometry (ξ_c)	2.3
RH of anode inlet (RH_a)	100%
RH of anode inlet (RH_c)	100%

Table 4
Physical properties.

Description	Value
Exchange current density × ratio of reaction surface to CL volume in anode side ($ai_{0,a}^{ref}$)	1.0×10^9 A m^{-3}
Exchange current density × ratio of reaction surface to CL volume in cathode side ($ai_{0,c}^{ref}$)	1.0×10^4 A m^{-3}
Activation energy for oxygen reduction reaction in cathode side (E_a)	73,269 J mol^{-1}
Reference hydrogen molar concentration ($c_{H_2,ref}$)	40.88 mol m^{-3}
Reference oxygen molar concentration ($c_{O_2,ref}$)	40.88 mol m^{-3}
Anodic and cathodic transfer coefficients for hydrogen oxidation reaction (HOR)	$\alpha_a = \alpha_c = 1$
Cathodic transfer coefficient for oxygen reduction reaction (ORR)	$\alpha_c = 1$
Dry membrane density (ρ^{mem})	2000 kg m^{-3}
Equivalent weight of electrolyte in membrane (EW)	1.1 kg mol^{-3}
Faraday constant (F)	96,487 C mol^{-1}
Universal gas constant (R_u)	8.314 J mol^{-1} K^{-1}
Surface tension (σ)	0.0625 N m^{-1}
Liquid water density (ρ^l (80 °C))	972 kg m^{-3}
Liquid water viscosity (μ^l)	3.5×10^{-4} N s m^{-2}

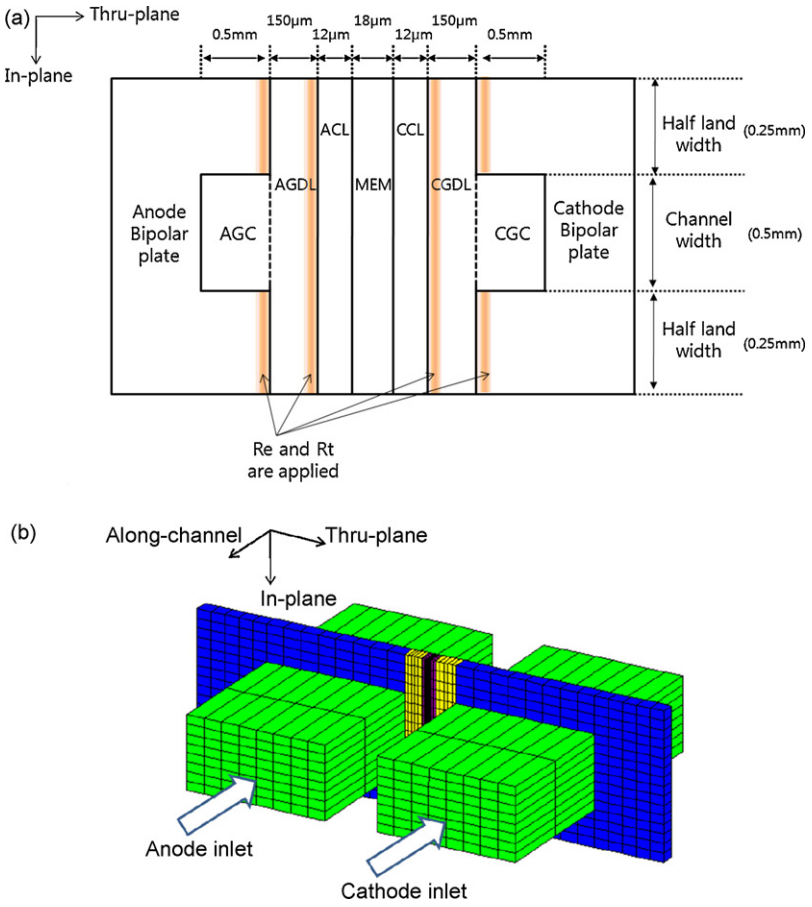

Fig. 2. Dimension of the PEFC two-dimensional cross-section geometry (a) and its mesh configuration (b) where the thermal and electronic contact resistances are applied at the GDL/CL interfaces and BP/GDL interfaces.

resistance at the GDL/CL interfaces is considered along the in-plane direction due to the differential clamping pressures that are applied at the gas channel and land regions, respectively. According to the experimental contact-resistance-pressure constitutive relation provided by Zhang et al. [28], the contact resistance between the BP and the GDL exponentially increases with decreasing champing pressure. Based on the experimental results, it is concluded that the contact resistance at the GDL/CL interface under the channel region is exponentially related to the distance from the edge of the land/channel as follows:

$$R_{chan} = R_{land} \cdot e^{3.5x} \tag{43}$$

In Eq. (43), x denotes the distance from the land/channel interface towards the channel region along the in-plane direction and the factor 3.5 is arbitrarily assumed. Based on the above assumption, the electronic and thermal contact resistances at the GDL/CL interface are plotted in Fig. 3 along the in-plane direction.

3.2. Simulation results

Fig. 4 displays the current density (I) and temperature (T) profiles in the membrane along the in-plane direction for three types of GDL, where PEFC operation at 1.5 A cm^{-2} is considered and the effects of both electronic and thermal contact resistances at the GDL/CL interfaces are ignored. Since the heat that is generated in PEFC is primarily removed through the GDL to the current-collector land of BP by lateral conduction (and thus, the land acts as a heat-sink for the GDL), the main heat-flow path is from inside CLs toward land regions. Consequently, for all three cases, higher temperature is predicted near the channel region due to a lack of effective cooling in the channel region. While the thru-plane GDL case leads to the greatest rise in membrane temperature due to its low GDL thermal conductivity (1.0 W m^{-1} K^{-1}), the difference between the temperature profiles of the in-plane and anisotropic GDL cases is relatively small. This indicates that an isotropic treatment using the in-plane GDL thermal conductivity leads to a smaller deviation in the temperature profile than the use of the thru-plane value. While the rise in the membrane temperature that corresponds to the anisotropic GDL is calculated to be roughly 2.1 °C, a rise of 4.1 °C in the maximum membrane temperature is predicted for the thru-plane GDL, which demonstrates a significant over-prediction of the rise in the membrane temperature in that case. On the other hand, the membrane temperature rises up to 1.3 °C for the in-plane GDL, which implies that the degree of under-prediction of the rise in the membrane temperature by the use of the in-plane thermal conductivity is relatively less serious. In addition, it is seen in Fig. 4 that the shape of the current density distribution in the membrane is considerably altered, when the rise in the local membrane temperature is significant. For both the in-plane and anisotropic GDLs, the current density is greater near the channel region. This indicates that the current density for both cases is mainly determined by the limitation in oxygen transport. In contrast to these two cases, the current density near the channels is lower for the thru-plane GDL and implies that significant membrane dehydration occurs due to the considerable over-prediction of the membrane temperature near the gas channels. Thus, ohmic loss is a dominant factor in the membrane current density and cell performance for the thru-plane GDL case.

Fig. 5 presents the current density and membrane temperature profiles for the same three GDL cases at 1.5 A cm^{-2} but the spatial

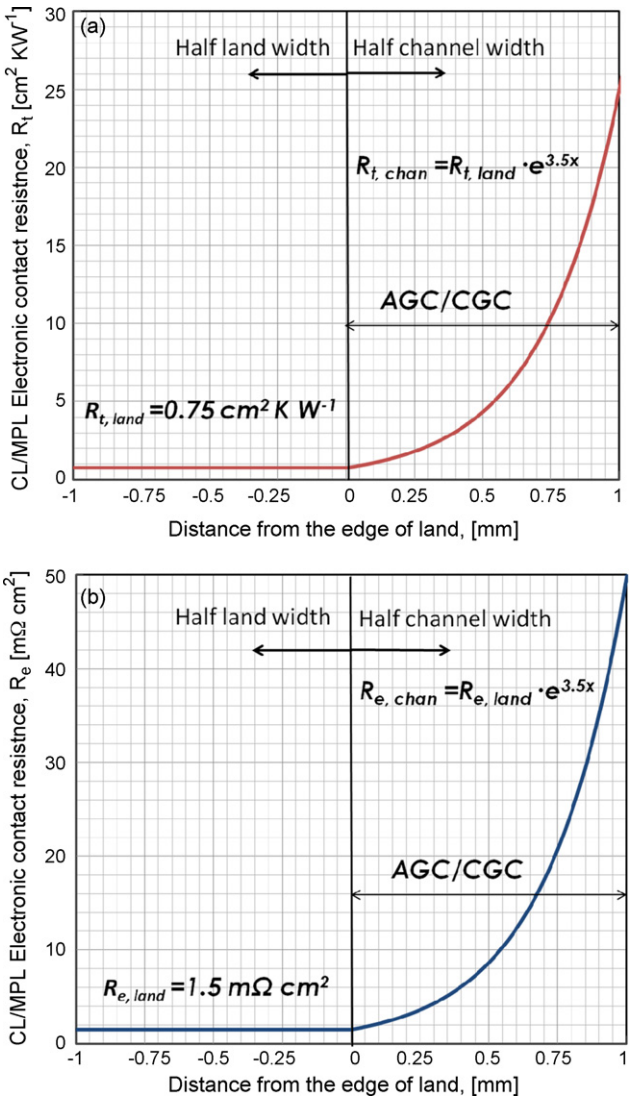

Fig. 3. Thermal contact resistance (a) and electric contact resistance (b) variations at the GDL/CL interfaces along the in-plane direction.

variation of electronic and thermal contact resistances between the GDL and CL is taken into account. A comparison of Fig. 5 with Fig. 4 clearly shows that the presence of contact resistance between the GDL and the CL (plotted in Fig. 3), results in a significant rise in temperature, particularly near the channel regions. For each GDL, the rise in temperature is predicted to be roughly 2 °C higher in Fig. 5 than in Fig. 4. The thermal effect also significantly alters the membrane current density profiles. For all three GDLs in Fig. 5, the current density near the land region becomes greater than that near the channel area, indicating that the membrane is not fully hydrated due to the higher rise in temperature. Thus the PEFC performance is determined mainly by the degree of membrane hydration. Consequently, in the three GDL cases, a lowered cell performance is seen in Fig. 5 due to the membrane dehydration effect as well as the electronic contact resistance between the GDL and the CL. The drop in performance is 31, 25, and 18 mV for the thru-plane, anisotropic, and in-plane GDL cases, respectively. The simulation results in Figs. 4 and 5 show that when both anode and cathode gas streams are fully humidified, the rise in the membrane temperature should be maintained within 2–3 °C to avoid significant membrane dehydration.

The membrane temperature and current density distributions at a lower current density, i.e., 0.5 A cm^{-2}, are presented in Fig. 6

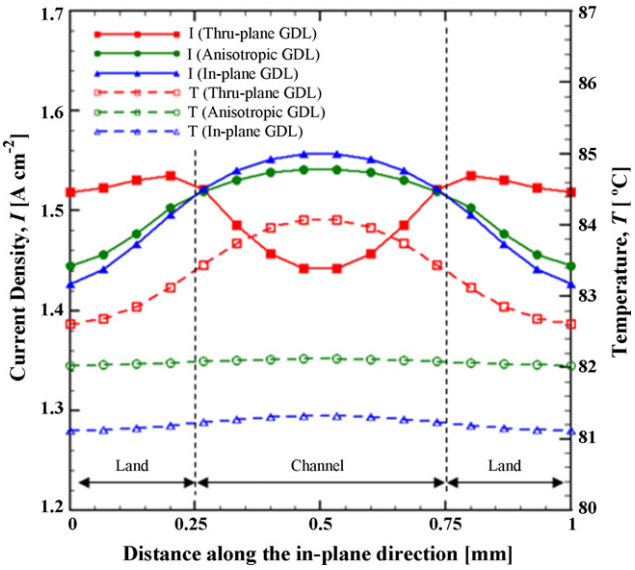

Fig. 4. Current density and temperature distributions in the membrane for the three GDL cases (I = 1.5 A cm^{-2} without the contact resistances at the GDL/CL and BP/GDL interfaces). Thru-plane GDL case: V_{cell} = 0.559 V: anisotropic GDL case: V_{cell} = 0.566 V: in-plane GDL case: V_{cell} = 0.566 V.

where the anisotropic and in-plane GDLs are considered without the effect of the contact resistance between the GDL and the CL. In addition, because the lower current density (0.5 A cm^{-2}) results in a lower gas velocity in the gas channels under a constant stoichiometry situation, a 15% coverage of the cathode GDL surface by liquid water is assumed to approximate the presence of water droplets at the cathode GDL/gas channel interface. Due to the low current density operation, the rise in membrane temperature is not significant, i.e., only 0.5 and 0.3 °C for the anisotropic and in-plane GDL cases, respectively. As a result, the membrane current density profiles for both cases are similar to each other, which indicates that the isotropic assumption for the GDL is reasonable in the case of low current density operation, e.g., 0.5 A cm^{-2}.

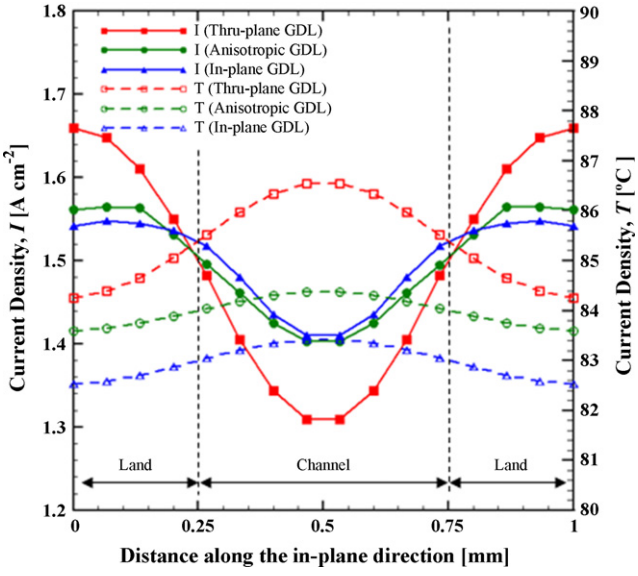

Fig. 5. Current density and temperature distributions in the membrane for the three GDL cases (I = 1.5 A cm^{-2} with the contact resistances at the GDL/CL and BP/GDL interfaces). Thru-plane GDL case: V_{cell} = 0.528 V: anisotropic GDL case: V_{cell} = 0.541 V: in-plane GDL case: V_{cell} = 0.548 V.

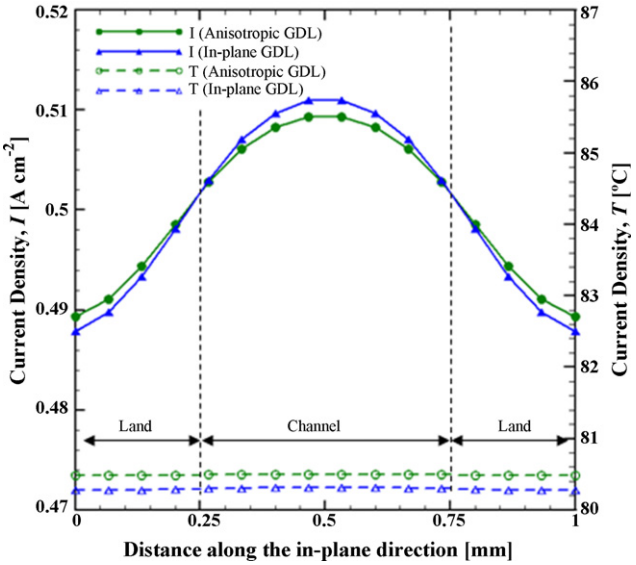

Fig. 6. Current density and temperature distributions in the membrane for the anisotropic and in-plane GDL cases ($I = 0.5\ A\ cm^{-2}$; without the contact resistances at the GDL/CL and BP/GDL interfaces; the 15% interfacial liquid droplet coverage is assumed at the cathode GDL/GC interface). Anisotropic GDL case: $V_{cell} = 0.709\ V$: in-plane GDL case: $V_{cell} = 0.708\ V$.

For the three cases presented in Fig. 4 (i.e., based on $1.5\ A\ cm^{-2}$ operation without contact resistance at the GDL/CL interfaces), Figs. 7 and 8, respectively, show the temperature and liquid saturation contours on the two-dimensional cross-section of the PEFC where the anode/cathode GDLs, anode/cathode CLs, and membrane are seen. As shown in Fig. 7, while a considerable rise in temperature (4.15 °C) occurs in the thru-plane GDL, there is a little difference in the temperature rises for the anisotropic and in-plane GDLs, i.e., 2.15 and 1.35 °C, respectively. On the other hand, the effect of GDL anisotropy is much more appreciable in terms of temperature contours. When the in-plane thermal conductivity is an order of magnitude larger than the thru-plane thermal conductivity, the temperature contour in the anisotropic GDL is more one-dimensional and varies more significantly in the thru-plane direction. Therefore, the isotropic and anisotropic GDLs exhibit vastly different thermal behaviour; this clearly demonstrates that the assumption of isotropic GDL thermal conductivity cannot provide realistic temperature distributions.

The liquid saturation contours for the same three GDL cases are presented in Fig. 8. Even with the same rate of water production that corresponds to the same current density, i.e., $1.5\ A\ cm^{-2}$, it is clearly seen that the liquid saturation profiles differ among the three GDLs, being strongly affected by the temperature profiles shown in Fig. 7. Due to the high rise of temperature in the thru-plane GDL, most of the water near the channel regions evaporates and water accumulates near the land region. On the other hand, water accumulates in a larger portion of the GDL for both the anisotropic and in-plane GDL cases, due to their relatively smaller rises of temperature.

It should be noted that two important phenomena emerge in the non-isothermal two-phase situation namely: (i) vapour-phase diffusion that is driven by the thermal gradient in the two-phase region and (ii) the heat-pipe effect due to the transfer of latent heat from evaporation in the catalyst layer (hot region) and recondensation over the current-collecting land (cold region). Both phenomena depend on the thermal gradient in the GDL between the hot and the cold regions. In the thru-plane and anisotropic GDLs, the reverse liquid saturation gradient is observed along the thru-plane direction from the current-collecting land side of GDL toward the CL side of GDL. This is due to the effect of relatively stronger vapour-phase diffusion that is driven by the larger thermal gradient. Consequently, the maximum liquid saturation for these two cases occurs near the surface of the interface of the GDL that faces the current-collecting land. On the other hand, the reverse liquid saturation gradient is not seen in the in-plane GDL because the vapour-phase diffusion is weak due to the small variation of temperature in the GDL. Therefore, the isotropic treatment that uses the value of the in-plane thermal conductivity fails to predict accurately the liquid saturation profile in the GDL by not capturing the reversed liquid saturation gradient that arises from the strong vapour-phase diffusion.

The temperature and liquid saturation contours with reference to the CL/GDL contact resistance are shown in Figs. 9 and 10, respectively. From a comparison of Figs. 7 and 9, it is clearly seen that the temperature gradient between the channel and land regions in GDL is greater in the case of Fig. 9 due to the variation of the contact resistance. The larger thermal gradient in Fig. 9 enhances vapour-phase diffusion and renders the level of liquid saturation near the land region higher. As a result, the maximum values of liquid saturation in the thru-plane and anisotropic GDLs in Fig. 10 are slightly higher than the maximum values in Fig. 8. An exceptional trend is seen in the in-plane GDL, where the rise in temperature without the GDL/CL contact resistance in Fig. 7 is minimal and thus facilitates the condensation of more water in the GDL due to the lower liquid

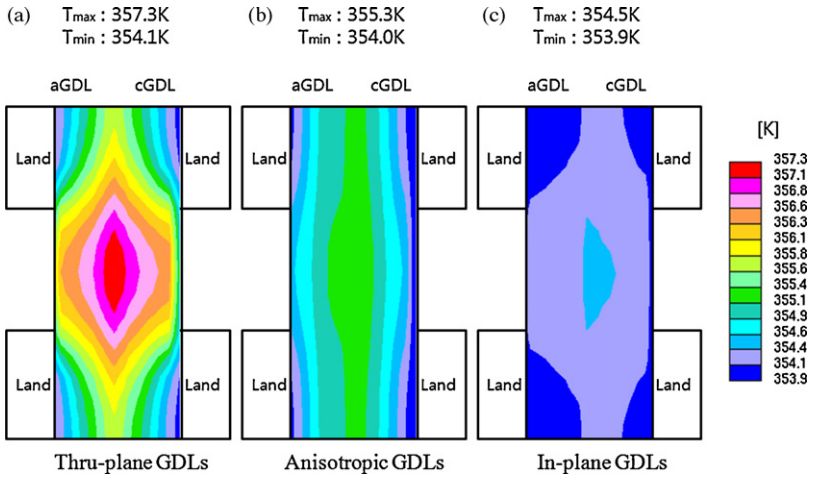

Fig. 7. Contours of temperature distributions in the two-dimensional cross-section of PEFC where the anode/cathode GDLs, anode/cathode CLs, and membrane are plotted ($I = 1.5\ A\ cm^{-2}$ without the contact resistances at the GDL/CL and BP/GDL interfaces).

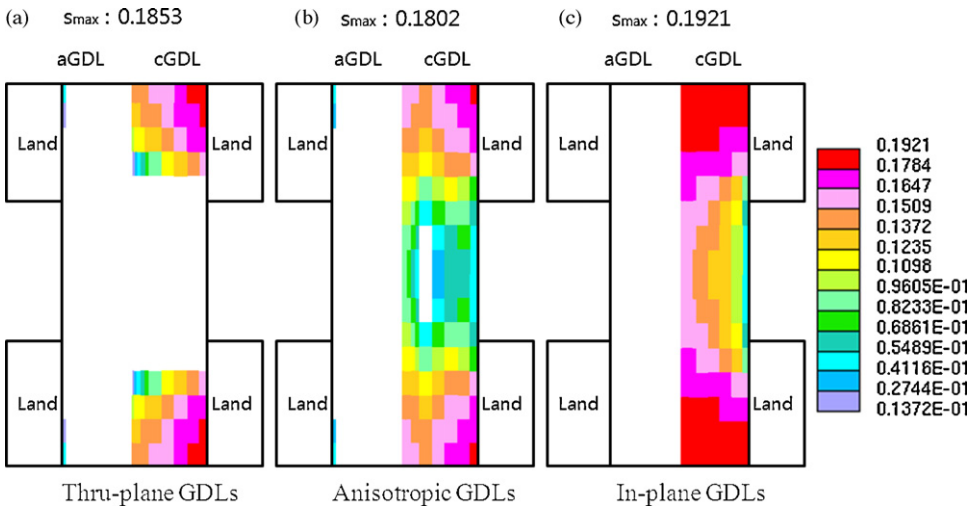

Fig. 8. Contours of liquid saturation distributions in the two-dimensional cross-section of PEFC where the anode/cathode GDLs, anode/cathode CLs, and membrane are plotted ($I = 1.5\ \mathrm{A\,cm^{-2}}$ without the contact resistances at the GDL/CL and BP/GDL interfaces).

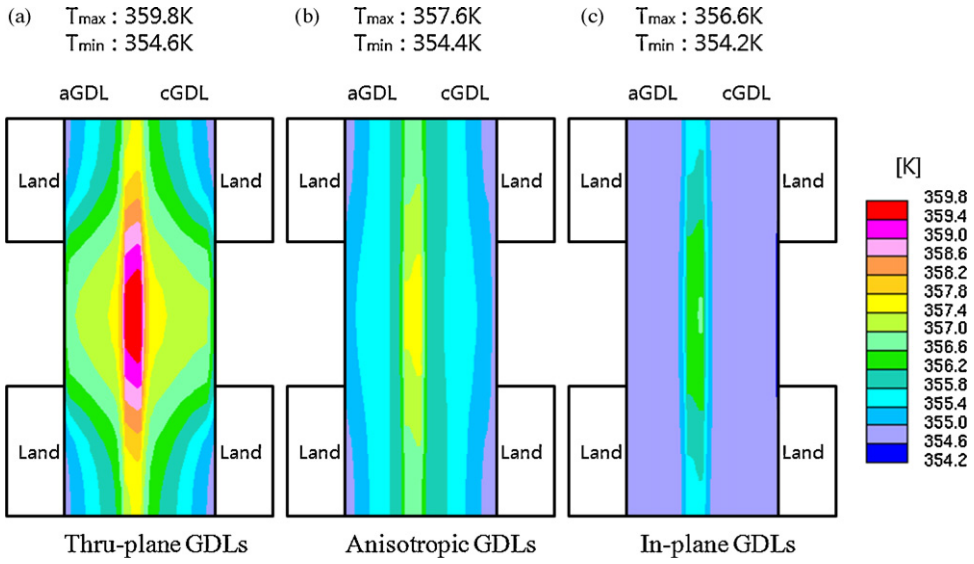

Fig. 9. Contours of temperature distributions in the two-dimensional cross-section of PEFC where the anode/cathode GDLs, anode/cathode CLs, and membrane are plotted ($I = 1.5\ \mathrm{A\,cm^{-2}}$ with the contact resistances at the GDL/CL and BP/GDL interfaces).

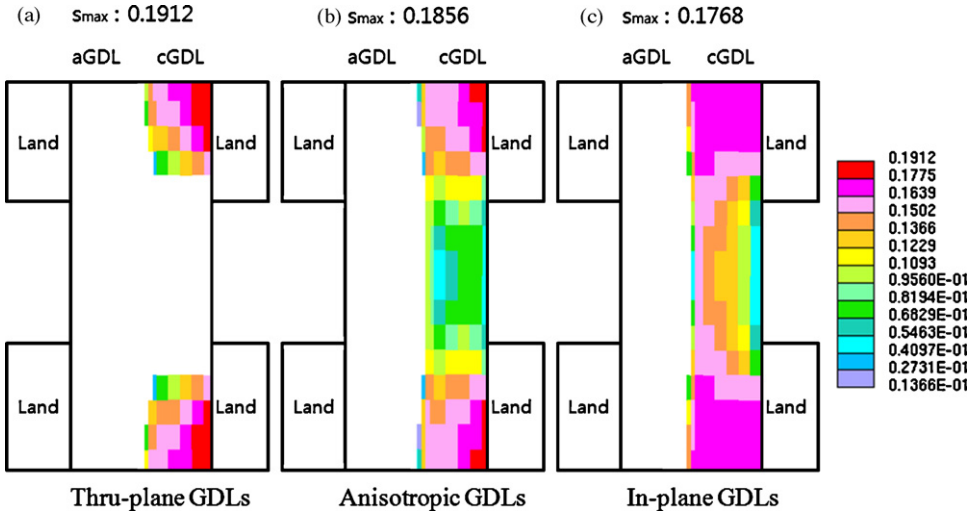

Fig. 10. Contours of liquid saturation distributions in the two-dimensional cross-section of PEFC where the anode/cathode GDLs, anode/cathode CLs, and membrane are plotted ($I = 1.5\ \mathrm{A\,cm^{-2}}$ with the contact resistances at the GDL/CL and BP/GDL interfaces).

saturation pressure, which increases the level of liquid saturation in GDL. Again, there is considerable difference in the liquid saturation profiles between the isotropic and anisotropic GDLs, which indicates a strong need to consider an anisotropic GDL in the modelling and simulation of PEFC.

4. Conclusions

Two-phase, non-isothermal simulations have been performed to assess the effects of an anisotropic GDL and the spatial variation of contact resistance between the CL and the GDL on the distribution of both temperature and water, as well as cell performance. The following conclusions can be reached.

1) The numerical results reveal vastly different thermal behaviour in the isotropic and anisotropic GDLs, and predict different temperature profiles due to the differences in the through-plane and in-plane GDL thermal conductivities. When the in-plane thermal conductivity is an order of magnitude larger than the through-plane thermal conductivity, the temperature profile in the anisotropic GDL is more one-dimensional, and varies more significantly in the thru-plane direction. Due to the strong interaction between the water and heat transport phenomena in a PEFC, different liquid saturation profiles between the anisotropic and isotropic GDLs are also captured by numerical simulations.
2) In terms of the rise of temperature in a PEFC, the maximum rise in the anisotropic GDL lies between two limits, where the lower and upper limits correspond to the isotropic GDLs that are designed as having the in-plane and through-plane thermal conductivities in all directions, respectively. Since the maximum temperature in the anisotropic GDL leans more toward the lower limit that is predicted in the in-plane GDL, it is concluded that isotropic treatment that uses the in-plane GDL thermal conductivity results in a smaller deviation in terms of the maximum rise in temperature than that which uses the thru-plane value.
3) Both the temperature and water distributions are considerably altered by the presence of contact resistance between the GDL and the CL, where the contact resistances at the GDL/CL interfaces are assumed to exponentially increase under the channel region due to the decreasing clamping pressures that are applied under gas channels. As a result, the temperature significantly increases near the channel regions and thus considerable membrane dehydration occurs. This significantly lowers both the membrane current density near the channel region and the overall PEFC performance. Vapour-phase diffusion is also enhanced due to the larger thermal gradient between the channel and land regions that is created by the variation in the contact resistance and results in a reversed liquid saturation gradient along the thru-plane direction.

Acknowledgements

Financial support for this work from Inha University is gratefully acknowledged. Thanks are also due to CD-adapco, Korea for their technical support for STAR-CD software.

References

[1] H. Ju, H. Meng, C.Y. Wang, Int. J. Heat Mass Transf. 48 (2005) 1303–1315.
[2] H. Ju, C.Y. Wang, S. Cleghorn, U. Beuscher, J. Electrochem. Soc. 152 (8) (2005) A1645–A1653.
[3] H. Ju, C.Y. Wang, Int. J. Automot. Technol. 9 (2) (2008) 225–232.
[4] P.K. Sinha, P.P. Mukherjee, C.Y. Wang, J. Mater. Chem. 17 (2007) 3089–3103.
[5] T.V. Nguyen, R.E. White, J. Electrochem. Soc. 140 (1993) 2178–2186.
[6] T.F. Fuller, J. Newman, J. Electrochem. Soc. 140 (1993) 1218–1225.
[7] J.S. Yi, T.V. Nguyen, J. Electrochem. Soc. 145 (1998) 1149–1159.
[8] M. Wöhr, K. Bolwin, W. Schnurnberger, M. Fischer, W. Neubrand, Int. J. Hydrogen Energy 23 (1998) 213–218.
[9] A. Rowe, X. Li, J. Power Sources 102 (2001) 82–96.
[10] G. Maggio, V. Recupero, C. Mantegazza, J. Power Sources 62 (1996) 167–174.
[11] S. Shimpalee, S. Dutta, Numer. Heat Transf.: Part A 38 (2000) 111–128.
[12] P. Costamagna, Chem. Eng. Sci. 56 (2001) 323–332.
[13] T. Berning, D.M. Lu, N. Djilali, J. Power Sources 106 (2002) 284–294.
[14] T. Zhou, H. Liu, I. J. Trans. Phenom. 3 (2001) 177–198.
[15] Y. Wang, C.Y. Wang, J. Electrochem. Soc. 153 (6) (2006) A1193–A1200.
[16] H. Ju, G. Luo, C.Y. Wang, J. Electrochem. Soc. 154 (2) (2007) B218–B228.
[17] G. Luo, H. Ju, C.Y. Wang, J. Electrochem. Soc. 154 (3) (2007) B316–B321.
[18] H. Meng, J. Power Sources 161 (2006) 466–469.
[19] U. Pasaogullari, P.P. Mukherjee, C.Y. Wang, K.S. Chen, J. Electrochem. Soc. 154 (8) (2007) B823–B834.
[20] C.J. Bapat, S.T. Thynell, J. Heat Transf. 129 (2007) 1109–1118.
[21] C.Y. Wang, P. Cheng, Int. J. Heat Mass Transf. 39 (1996) 3607–3618.
[22] R.B. Bird, W.E. Stewart, E.N. Lightfood, Transport Phenomena, John Wiley & Sons, New York, 1960.
[23] R.E. Meredith, C.W. Tobias, in: C.W. Tobias (Ed.), Conduction in Heterogeneous Systems, Advances in Electrochemistry and Electrochemical Engineering 2, Interscience Publishers, New York, 1962.
[24] T.E. Springer, T.A. Zawodinski, S. Gottesfeld, J. Electrochem. Soc. 136 (1991) 2334–2341.
[25] C. Berger, Handbook of Fuel Cell Technology, Prentice-Hall, New Jersey, 1968.
[26] A. Parthasarathy, S. Srinivasan, A.J. Appleby, J. Electrochem. Soc. 139 (1992) 2530–2537.
[27] CD-Adapco Group, STAR-CD Version 3.15 Methodology, CD-Adapco Group, USA, 2001.
[28] L. Zhang, Y. Liu, H. Son g, S. Wang, Y. Zhou, S.J. Hu, J. Power Sources 162 (2006) 1165–1171.